

Three Dimensional Printed Vertically-Stacked Single-/Multi-Band Coaxial Filters and RF Diplexers

Kunchen Zhao¹, *Graduate Student Member, IEEE*, and Dimitra Psychogiou², *Senior Member, IEEE*

Abstract—This article reports on monolithically integrated and low form-factor vertically-stacked coaxial resonator-based single-/multi-band filters and radio frequency (RF) diplexers using stereolithography apparatus (SLA) additive manufacturing (AM). The proposed RF filtering/diplexer concepts exhibit the following unique features: 1) low form-factor due to the use of vertically stacked low-profile capacitively-loaded coaxial cavity resonators; 2) monolithic integration; and 3) versatile and highly selective transfer functions facilitated by the topological arrangements of the resonators within the filter volume that enable cross-couplings and can be exploited to increase selectivity. Theoretical filter design analysis using coupling routing diagrams (CRDs) and eigen-mode electromagnetic (EM) simulations are performed. The proposed concept is validated by the design, fabrication, and testing of four monolithically-integrated prototypes, namely a four-pole two transmission zeros (TZs) bandpass filter (BPF), a three-pole two TZs BPF, a second-order dual-band BPF, and a second-order diplexer operating at C-band and exhibiting an effective quality factors (Q_{effs}) > 700.

Index Terms—Additive manufacturing (AM), bandpass filter (BPF), coaxial filter, diplexer, miniaturized filter, multiband filter, 3-D printing, transmission zero (TZ).

I. INTRODUCTION

THE fast growing pace of modern multiservice communication systems has posed new challenges for spectrum-efficient, low-profile, and cost-efficient radio frequency (RF) transceivers [1]. In these systems, bandpass filters (BPFs) play a key role in enhancing the signal-to-noise ratio (SNR) by selecting the desired signal of interest while suppressing the out-of-band interference and noise. To effectively serve the needs for ground-based and space-based communication systems, both performance and size requirements need to be met, which are summarized in the rest of this section.

High selectivity is typically obtained by incorporating the BPFs multiple resonators to achieve higher-order transfer functions. However, this approach results in large physical size and higher levels of insertion loss (IL). Yet another

method to obtain a sharp skirt is to introduce transmission zeros (TZs) near the passband. They can be generated using mixed electromagnetic (EM) coupling elements [2], [3], nonresonating modes [4], [5], and strongly-coupled triplets [6], [7], [8]. Specifically, in coaxial cavity resonator-based filters that are preferred in base-station systems due to their high-quality factor (Q), small size and wide spurious-free range [9], [10], TZ generation is obtained by introducing cross couplings [11], [12], [13]. However, this approach usually results in sensitive filter implementations or bulky and complicated geometrical features that require multiple computer numerical control (CNC) machined parts to be manufactured and assembled. For instance, the filter in [12] requires two metal parts to be machined with more than 30 assembly and tuning screws.

Multiband operability is a key required functionality for the next generation of multistandard configurations and can only be enabled by incorporating multiband filters in the RF front-end. However, the majority of the multiband BPF configurations to date are implemented using planar printed circuit board (PCB)-based or substrate-integrated waveguide (SIW) [14], [15], [16] topologies that suffer from high IL (e.g., 3–4.3 dB in [15]). Metal waveguide resonator-based multiband BPFs have also been proposed [17] to reduce IL. Nevertheless, they are really large in size. For instance, the size of a single rectangular cavity resonator is $0.93 \times 0.41 \times 0.76 \lambda_0^3$ in [17]. Multiband coaxial cavity filters are on the other hand significantly smaller. Notable examples of these approaches include the dual-capacitively loaded coaxial resonators in [18] and [19] and the stepped impedance resonator approach in [20] and [21]. Dual-band coaxial cavity filters using dual-mode coaxial cavity resonators with double ground plane [22], intermediate conductors [23], and stub-loaded resonators [24] have also been proposed. However, they are all implemented using a split block approach where multiple CNC machined parts are assembled with screws thus increasing the manufacturing complexity, size, and weight.

Size compactness is another fundamental requirement for 3-D RF front ends in which high- Q filters are of critical importance. It is typically addressed by incorporating in their RF front-ends coaxial cavity resonator filters that exhibit smaller volumes than their rectangular waveguide counterparts due to the capacitive loading of the resonator post [25]. To further reduce the size of such types of filters, distributed coaxial resonator BPF architectures have been proposed in [26] and [27]. However, the majority of them are based on

Manuscript received 6 March 2023; revised 12 April 2023; accepted 17 April 2023. Date of publication 11 May 2023; date of current version 6 November 2023. This work was supported by the Science Foundation Ireland (SFI) under Grant 20/RP/8334. (Corresponding author: Kunchen Zhao.)

Kunchen Zhao is with the Department of Electrical, Computer and Energy Engineering, University of Colorado Boulder, Boulder, CO 80309 USA (e-mail: kunchen.zhao@colorado.edu).

Dimitra Psychogiou is with the Department of Electrical and Electronic Engineering, University College Cork, Cork, T12 K8AF Ireland, and also with the Tyndall National Institute, Cork, T12 R5CP Ireland (e-mail: dpsychogiou@ucc.ie).

Color versions of one or more figures in this article are available at <https://doi.org/10.1109/TMTT.2023.3269522>.

Digital Object Identifier 10.1109/TMTT.2023.3269522

in-line configurations, i.e., all of the resonators are placed in the same plane. To effectively use the available 3-D volume of an RF system, vertically-stacked resonator arrangements can be considered [22], [28], [29], [30], [31]. For instance, in [22], an extra cavity is added on top of a coaxial resonator to create a dual-band transfer function. While this approach resulted in a significantly more compact volume, it is based on multiple CNC machined parts that need to be manufactured and postassembled and result in higher fabrication cost and additional weight and volume due to the need for assembly screws.

Although significant research efforts have been conducted to address all of the aforementioned challenges individually, none of the existing 3-D coaxial filtering configurations can satisfy all of these requirements simultaneously. As such, new design, integration, and manufacturing solutions are currently being sought. In terms of manufacturing, digital additive manufacturing (AM) technologies or 3-D printing are increasingly being investigated as a low-cost rapid prototyping alternative to traditional CNC machining. Furthermore, their free-form manufacturing capabilities could be exploited to create novel RF filtering topologies with enhanced functionality and improved RF performance. Metal-based AM processes such as direct metal laser sintering (DMLS) [32], selective laser sintering (SLM) [33], and electron beam melting (EBM) [34] have been proposed for prototyping waveguide-based RF passive components and are potentially suitable for monolithic integration. However, the cost of the metal-based AM process is still high, and the performance of the metal 3-D printed devices usually suffers from poor surface roughness [35].

Plastic/resin-based 3-D printing such as stereolithography apparatus (SLA) [36], [37], [38], [39], fused deposition modeling (FDM) [40], [41], and lithography-based ceramic manufacturing (LCM) [42] result in better surface roughness and significantly lower cost. However, the majority of the existing monolithic plastic-based AM process has been used for the realization of open-ended waveguide-based structures due to the challenge of internal metallization. On the other hand, coaxial resonator-based devices are mostly manufactured using split-block approaches [43], [44], which result in higher weight and volume due to the assembly screws and radiation loss which led to a high IL in the BPF e.g., 1.3 dB in [28]. Recently, a monolithic integration concept of coaxial cavity resonators using SLA 3-D printing has been proposed for the realization of BPFs with TZ, extended spurious-free range, multiband functionality, and co-design of the filtering antenna [45], [46], [47], [48], [49].

In this article, monolithically-integrated vertically-stacked SLA-based single- and multiband coaxial RF BPFs and diplexers are proposed and experimentally validated. Enabled by SLA-based 3-D printing, monolithic monoblock integration of vertically-stacked quasi-elliptic BPFs and RF diplexers is demonstrated for the first time. The proposed RF filtering technologies exhibit the following unique features: 1) low form-factor due to the use of vertically stacked, low-profile capacitively-loaded coaxial cavity resonators and due to their monolithic integration; 2) multiple TZs that increase the selectivity of the filter thanks to the space

arrangement of the resonators that enable the realization of cross-couplings; and 3) versatile single band and dual-band quasi-elliptic transfer functions that are realized with 3-D coaxial high- Q resonators. Compared to the authors' previous work in [45], [46], [47], [48], [49], the filtering architectures in this manuscript demonstrate a higher level of geometrical complexity where vertical-stacking, cross-couplings, electrical/magnetic couplings, and novel external coupling structures are combined within a monolithically-integrated RF component. Furthermore, advanced transfer-functions are uniquely demonstrated using compact monolithically-integrated coaxial resonators. To validate the proposed concept, a four-pole two TZs BPF, a three-pole two TZs BPF, a second-order dual-band BPF and a second-order diplexer operating at C -band were designed, manufactured, and tested.

The manuscript is structured as follows. In Section II, the theoretical filter design methodology is discussed by presenting the operating principles of the fundamental coupling routing diagrams (CRDs). In Section III, full-wave eigenmode analysis is performed to specify the geometrical characteristics of realistic coupling structures. Section IV presents the manufacturing aspects and RF-measured performance parameters of the filter prototypes and Section V reports on the major contributions of this work.

II. THEORETICAL FOUNDATION

In this section, the operating principles of four different filtering architectures are discussed through their CRDs and their corresponding synthesized responses. These include a four-pole two TZs BPF, a three-pole two TZs BPF, a second-order dual-band BPF, and a second-order diplexer.

A. Four-Pole Two-TZ BPF

The CRD of the four-pole two-TZ BPF is shown in Fig. 1(a). It comprises four synchronously-tuned resonators that generate four poles and two TZs, TZ_1 , and TZ_2 . Both of the TZs are generated by the cross-coupling m_{14} between resonators 1 and 4 which needs to have a different sign from the one assigned for m_{12} , m_{23} , and m_{34} . The synthesized power transmission and reflection response in the normalized frequency (Ω) domain of the four-pole two-TZ BPF is depicted in Fig. 1(b). As can be seen, the two TZs are generated near the passband, creating a highly-selective transfer function. The location of the TZs and the out-of-band rejection can be altered by changing the strength of the cross-coupling m_{14} . In particular, lower values of m_{14} move the TZs away from the passband and result in higher out-of-band rejection (see example 1) at the expense of roll-off.

B. Three-Pole Two-TZ BPF

The details of the three-pole/two-TZ CRD are shown in Fig. 2(a). The proposed filter configuration consists of two sections, namely a two-resonator section comprised of resonators 1 and 2 and a one-resonator section shaped by resonator 3. Both sections are coupled to the source and the load via external coupling elements. In this CRD configuration,

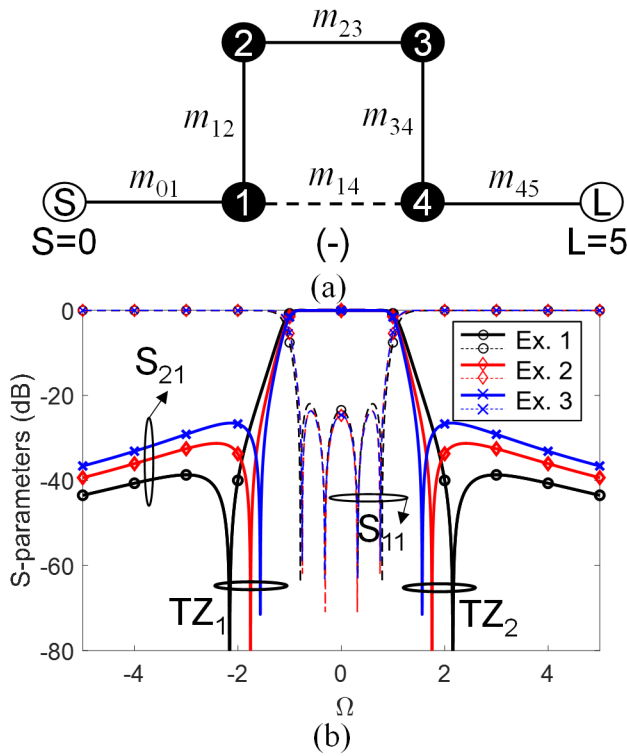


Fig. 1. (a) CRD of the four-pole two-TZ BPF. Black circles: resonating nodes, white circles: source and load, solid line: positive coupling, and dashed line: negative coupling. (b) Synthesized response of the four-pole two-TZ BPF with different m_{14} values showing TZ control. The coupling coefficients are example 1: $m_{01} = m_{45} = 1$, $m_{12} = 0.8$, $m_{23} = 0.66$, and $m_{14} = -0.1$; example 2: $m_{01} = m_{45} = 1$, $m_{12} = 0.775$, $m_{23} = 0.66$, and $m_{14} = -0.15$; and example 3: $m_{01} = m_{45} = 1$, $m_{12} = 0.76$, $m_{23} = 0.68$, and $m_{14} = -0.2$.

the self-coupling coefficients $m_{11} = m_{22} \neq m_{33}$ need to be different for the desired three-pole/two-TZ response to be obtained. As shown in Fig. 2(b), the location of the TZ_2 can be tuned independently by altering the external coupling to resonator 3, m_{03} , where larger m_{03} s moves the TZ away from the passband. Fig. 2(c) shows the synthesized response of the BPF when the frequency of the resonator 3 (self-coupling coefficient m_{33}) is altered. As shown, m_{33} affects both the BW of the passband and the location of the TZs. In particular, the BW will increase and the location of the two TZs will be closer when resonator 3 is tuned to higher frequencies [see example 1 in Fig. 3(c)]. Therefore, the location of the TZs and the BW can be arbitrarily designed by appropriately selecting m_{03} and m_{33} .

C. Second-Order Dual-Band BPF

Fig. 3(a) demonstrates the CRD of the second-order dual-band BPF and its corresponding power transmission and reflection responses are depicted in Fig. 3(b). The dual-band response is created by two second-order filtering sections with different center frequencies. In particular, the low-frequency section consists of resonators 1, 2, and the high-frequency section consists of resonators 3, 4. In order to increase the isolation between the passbands, the sign of the inter-resonator coupling between the two paths must be set opposite to create a TZ. In this case, m_{12} is set to be positive and m_{34} is set

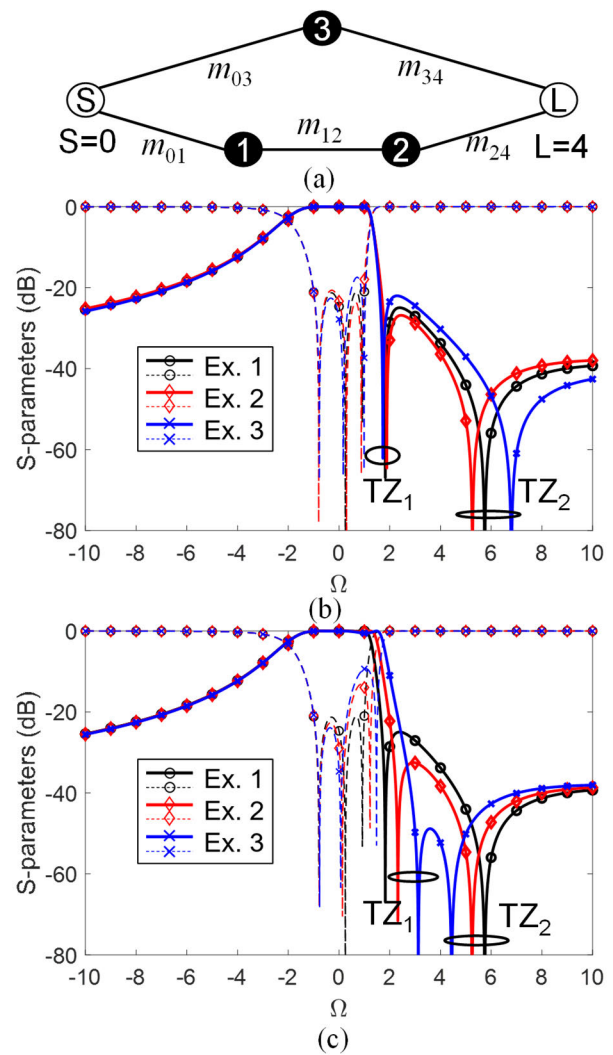


Fig. 2. (a) CRD of the three-pole/two-TZ BPF. (b) Synthesized response of the three-pole/two-TZ BPF for different values of m_{03} . Example 1: $m_{03} = m_{34} = 0.36$; example 2: $m_{03} = m_{34} = 0.38$; example 3: $m_{03} = m_{34} = 0.39$, and for all examples, $m_{01} = m_{24} = 1.06$, $m_{12} = 1.12$, $m_{11} = m_{22} = 0.48$, and $m_{33} = -1.35$. (c) Synthesized response of the three-pole/two-TZ BPF for different values of m_{33} . Example 1: $m_{33} = -1.35$; example 2: $m_{33} = -1.55$; example 3: $m_{33} = -1.75$, and for all examples, $m_{01} = m_{24} = 1.06$, $m_{12} = 1.12$, $m_{11} = m_{22} = 0.48$, and $m_{03} = 0.38$.

to be negative. The center frequency of each band can be configured independently by altering the resonator frequency at each filtering section as demonstrated in examples 1–3 in Fig. 3(b).

D. Second-Order Diplexer

The CRD of the second-order RF diplexer is depicted in Fig. 4(a). In this case, each of the high- and low-frequency filtering sections is connected to an output load to create the diplexer response. The signs of all the coupling elements are identical. The synthesized power transmission and reflection response of the second-order diplexer are shown in Fig. 4(b). Similar to the dual-band BPF example, both filtering sections can be tuned independently by altering the frequency of the resonator in different sections as illustrated in examples 1–3 in Fig. 4(b).

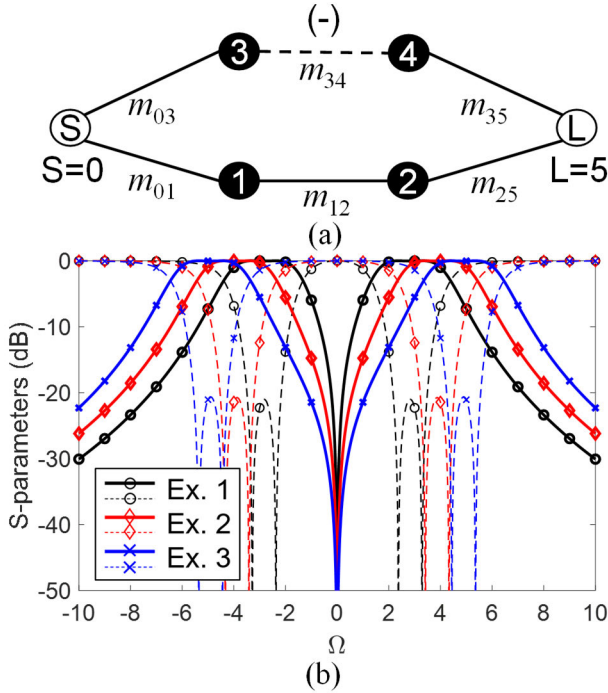


Fig. 3. (a) CRD of the second-order dual-band BPF. (b) Synthesized response of the second-order dual-band BPF for different values of the resonator frequencies (m_{xx}). Example 1: $m_{11} = m_{22} = 3$ and $m_{33} = m_{44} = -3$; example 2: $m_{11} = m_{22} = 4$ and $m_{33} = m_{44} = -4$; example 3: $m_{11} = m_{22} = 5$ and $m_{33} = m_{44} = -5$, for all examples $m_{01} = m_{03} = m_{45} = m_{25} = 1$ and $m_{12} = m_{34} = 1.1$.

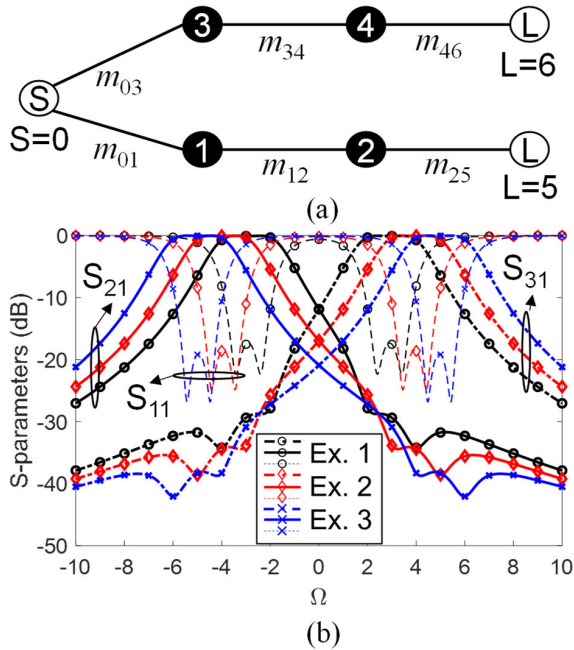


Fig. 4. (a) CRD of the second-order diplexer. (b) Synthesized response of the second-order diplexer for different self-coefficient values (m_{xx}). Example 1: $m_{11} = m_{22} = 3$ and $m_{33} = m_{44} = -3$; example 2: $m_{11} = m_{22} = 4$ and $m_{33} = m_{44} = -4$; example 3: $m_{11} = m_{22} = 5$ and $m_{33} = m_{44} = -5$, and for all examples $m_{01} = m_{03} = 1$, $m_{46} = m_{25} = 1$, and $m_{12} = m_{34} = 1.1$.

III. COUPLING STRUCTURES DESIGN FOR COAXIAL-RESONATOR-BASED INTEGRATION

To physically realize the aforementioned CRDs using coaxial-cavity resonators while occupying the smallest

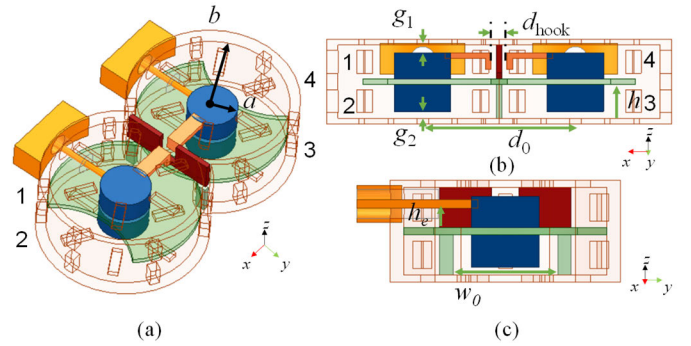


Fig. 5. (a) Geometry of the four-pole/two-TZ BPF based on the CRD in Fig. 1. (b) Front-view. (c) Side view. Geometrical parameters: $a = 5$; $b = 15$; $h = 6$; $g_1 = 1.38$; $g_2 = 1.2$; $d_0 = 21.2$; $h_e = 3.55$; $d_{\text{hook}} = 2.4$; and $w_0 = 15.4$, all units are in mm.

possible volume, novel coupling structures and geometrical configurations aiming to minimize the 3-D volume of an RF component need to be considered. Specifically, coupling elements allowing for vertically-stacked resonators as opposed to conventional in-line-based integrations are being sought to reduce the filter's form factor and allow for cross-couplings. To better characterize the size compactness and effective use of a given 3-D volume, the metric of the axial ratio (AR) of a 3-D object can be used and defined as follows:

$$\text{AR} = \frac{\text{Maxsizeinx} - \text{yplane}}{\text{HeightinZaxis}}. \quad (1)$$

Based on (1), the minimum achievable AR for a 3-D BPF is the one obtained when the BPF exhibits a cubical shape and is equal to $\sqrt{2}$. Therefore, all of the proposed practical realization schemes for the CRDs in Figs. 1–3 are aimed toward an AR as close as possible to $\sqrt{2}$.

A. Four-Pole Two-TZ BPF

Fig. 5 shows the detailed geometry of the four pole/two TZ BPF designed for a center frequency of 4 GHz and a fractional bandwidth (FBW) of 6.5% and using as a basis the CRD in Fig. 1. It is comprised of four resonators (labeled as resonators 1–4 in Fig. 1) that are placed in two vertically stacked resonator pairs. For the CRD to be physically realizable, three different inter-resonator coupling configurations need to be developed, namely the: 1) vertical inductive coupling that is applied between resonators 1, 2, and 3, 4; 2) horizontal iris-based inductive coupling applied between resonators 2 and 3; and 3) the capacitive cross-coupling that is used between resonators 1 and 4 for the TZs to be generated. The external coupling in this geometrical configuration is obtained by directly tapping the SMA probe to the post of resonators 1 and 4. Specific details on the geometrical and operating principles of each of these couplings are provided below.

1) *Inter-Resonator Coupling: Vertically-Stacked:* In order to achieve a compact form factor by reducing the AR of the filter, vertically-stacked resonators can be used as shown in Fig. 6(a) [30]. The two resonators are arranged in a back-to-back configuration with a shared ground in the xy plane. The resonators are inductively coupled with an opening in their shared ground plane. This opening is obtained by subtracting

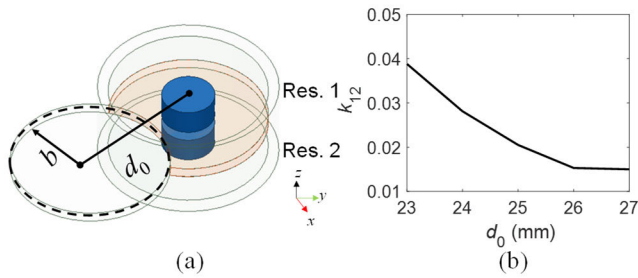


Fig. 6. (a) Eigen-mode model of two vertically stacked coaxial cavity resonators. The coupling window is materialized by subtracting from the shared ground plane a circular patch with a radius of b and distance d_0 from the cavity center. (b) Simulated inter-resonator coupling k_{12} for different d_0 .

a circular patch with a radius of b and distance d_0 from the cavity center. In this manner, the size of the coupling window can be controlled by altering the distance d_0 . The inter-resonator coupling coefficient k_{ij} can be defined as

$$k_{ij} = m_{ij} \cdot \text{FBW} \quad (2)$$

where m_{ij} is the normalized coupling coefficient and FBW is the fractional bandwidth of the filter. The extracted inter-resonator coupling coefficient k_{12} is shown in Fig. 6(b). As can be seen, higher values of k_{12} can be obtained with lower d_0 i.e., a larger coupling window.

2) *Inter-Resonator Coupling: Horizontal:* Horizontal iris-based coupling is used in coaxial cavity-based filters to obtain inductive-type inter-resonator coupling in in-line resonator configurations. This coupling scheme has been quantitatively studied in [46]. The coupling strength is mainly controlled by the distance between the adjacent resonators and the width of the iris, where a lower distance or larger iris width results in larger coupling coefficients. In the case of the proposed four-pole/two-TZ BPF, the horizontal iris coupling is applied between resonators 2 and 3 as shown in Fig. 5.

3) *Inter-Resonator Coupling: Capacitive Coupling:* Capacitive couplings are highly desirable in filtering configurations when negative inter-resonator coupling coefficients are needed for example for the realization of m_{14} in Fig. 1. Fig. 7(a) and (b) shows the proposed capacitive coupling scheme. It is provided through a pair of metallic hooks that are connected to the center post of the resonators. At resonance, an electric (E) field will be established between the surfaces of the adjacent hooks, resulting in the capacitive coupling between the two resonators. In addition, the two resonators are isolated by a metal wall to minimize the amount of inductive coupling. The extracted coupling coefficient using eigen-mode simulation is shown in Fig. 7(b). As can be seen, the coupling strength is mainly controlled by the distance between the surfaces of the metal hooks d_{hook} , where the larger coupling is obtained for small d_{hook} s.

4) *External Coupling: Direct Tapping:* The external coupling is obtained by directly connecting the SMA probe to the post of resonators 1 and 4 as shown in Fig. 5. The strength of the external coupling coefficient (Q_{ext}) is altered by modifying the height of the tapping location h_e [see Fig 5(c)], where the larger value of h_e results in smaller Q_{ext} as also discussed in [46].

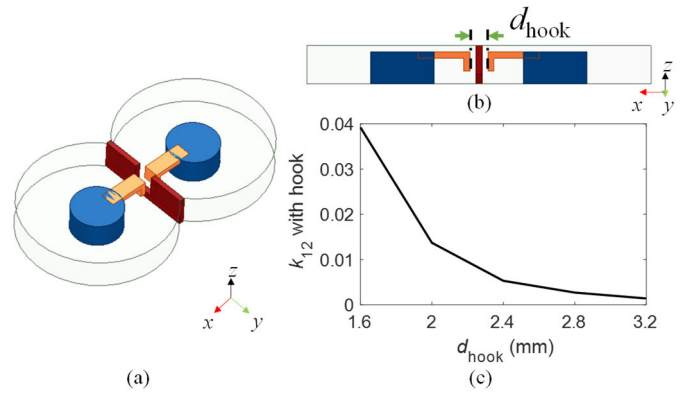


Fig. 7. (a) Eigen-mode simulation model to extract the inter-resonator coupling k_{12} of two horizontally capacitive-coupled coaxial cavity resonators. Capacitive coupling is achieved by a pair of conductive hooks between the resonator posts. (b) Side view of the capacitive coupled resonators. (c) Simulated inter-resonator coupling k_{12} with different d_{hook} .

5) *Axial Ratio:* Considering the operating principles and geometrical details of the 3-D coupling elements, the filter dimensions can be specified for the desired center frequency (4 GHz) and FBW (6.5 %) and are provided in Fig. 5. In this case, the resulting AR is calculated around 4.07. Although it appears to be larger than the minimum desired AR of $\sqrt{2}$, it is significantly smaller than the AR of a conventional four-pole in-line BPF using the same coaxial-cavity resonator which has an AR over 13.

B. Three-Pole Two-TZ BPF

Fig. 8 shows the detailed geometry of the three-pole/two-TZ BPF that is designed for a center frequency of 4.5 GHz and FBW of 16% using as a basis the CRD in Fig. 2. It is comprised of three resonators (labeled as res 1–3), where resonator 3 is located on top of resonators 1 and 2. An elliptically-shaped outer cavity is used for this resonator to comply with the overall volume occupied by the bottom resonators leading to an AR of 3.72. Note that the elliptically-shaped outer cavity wall does not change the fundamental mode of the resonator. A horizontal iris-based inductive coupling is applied between resonators 1 and 2. It should be noticed that resonators 1 and 3 need to be excited simultaneously to achieve the desired transfer function. Therefore, a novel U shape external coupling network needs to be developed.

1) *External Coupling: U-Shape:* Conventionally, the external coupling to a coaxial cavity resonator is achieved by directly tapping the SMA probe to the post or by vertically inserting the SMA probe inside the cavity. Nevertheless, those approaches are not applicable when two resonators need to be excited simultaneously e.g., in the case of the three-pole two-TZ BPF in Fig. 2 and the dual-band BPF and diplexer in Figs. 3 and 4. Therefore, a novel external coupling structure for vertically stacked coaxial cavities is proposed and is shown in Fig. 9(a) and (b). Specifically, the coupling network is comprised of a U-shaped metal conductor (highlighted in red) attached to the center post of the two resonators. The SMA probe is connected to the center of the coupling network. In this example case, the two resonators are chosen to resonate

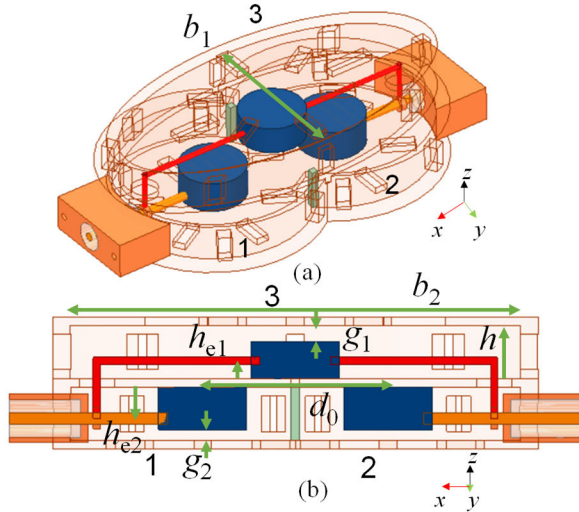


Fig. 8. (a) Geometry of the three-pole/two-TZ BPF, the CRD is shown in Fig. 2. (b) Side view. Geometry values are $b_1 = 25.9$, $b_2 = 51.8$, $h = 6$, $g_1 = 2$, $g_2 = 1.2$, $d_0 = 21.8$, $h_{e1} = 2$, and $h_{e2} = 3.5$, all units are in mm.

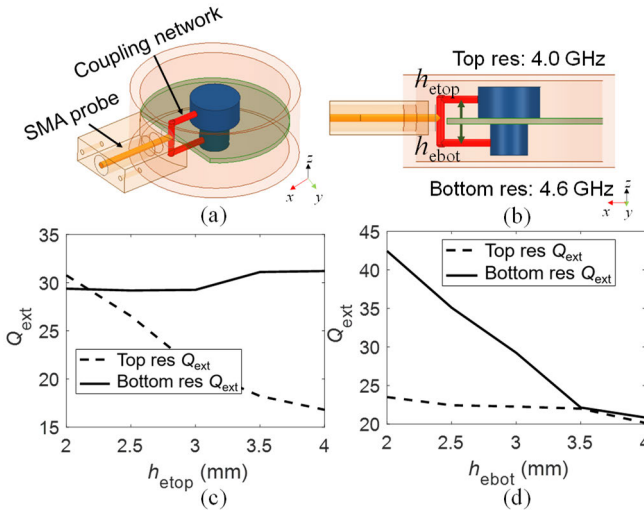


Fig. 9. (a) EM model of the U-shaped external coupling network for two resonators resonating at 4.0 and 4.6 GHz. (b) Side-view. (c) External coupling Q_{ext} of the two resonators for different h_{etop} . (d) Q_{ext} of the two resonators with different h_{ebot} .

at different frequencies, where the top resonator is set at 4.0 GHz and the bottom one at 4.6 GHz.

Fig. 8(c) and (d) shows the extracted Q_{ext} , which is calculated using

$$Q_{\text{ext}} = \frac{1}{m_{01}^2 \cdot \text{FBW}} \quad (3)$$

where m_{01} is the normalized coupling coefficient. As it can be seen, the external coupling for both of the resonators can be independently tuned by changing the height of the coupling structures, namely h_{etop} and h_{ebot} . In particular, a larger value of h_{etop} will result in lower Q_{ext} for the top resonator, while the Q_{ext} of the bottom resonator remains unaffected. Similarly, increasing h_{ebot} will cause the Q_{ext} of the bottom resonator to be reduced, while the Q_{ext} of the top resonator remains about the same.

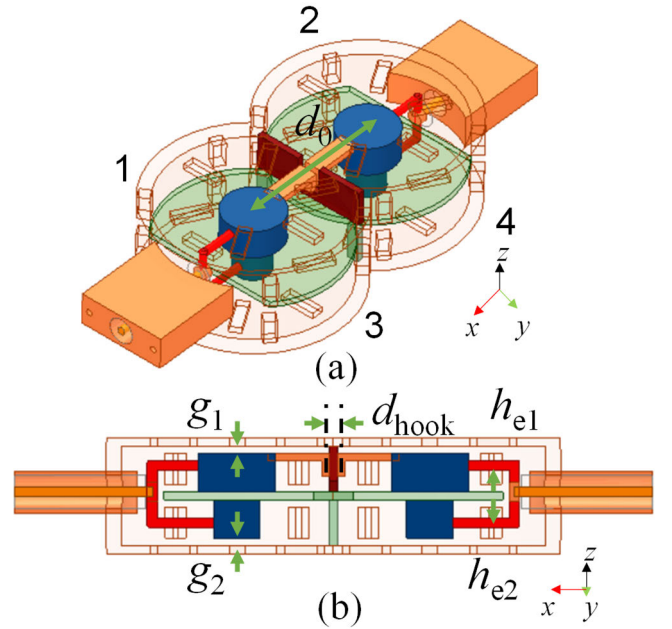


Fig. 10. (a) Geometry of the second-order dual-band BPF based on the CRD in Fig. 3. (b) Side view. Geometrical parameters: $a_1 = 5$; $a_2 = 3$; $h = 6$; $g_1 = 1.2$; $g_2 = 1.2$; $d_0 = 25$; $h_{e1} = 3.5$; $h_{e2} = 3$; and $d_{\text{hook}} = 2.2$, all units are in mm.

C. Second-Order Dual-Band BPF

Fig. 10 shows the detailed geometry of second-order dual-band BPF based that is designed based on the CRD in Fig. 3. Its bands are centered at $f_1 = 4.0$ GHz and $f_2 = 4.65$ GHz, respectively. The designed FBW is 8% for the lower band and 7.3% for the higher band. The dual-band BPF is arranged so that a minimum AR of 3.93 is obtained by vertically stacking its single-band counterparts with each part comprising two horizontally iris-coupled resonators. The low-frequency part is placed in the upper half of the filter (resonators 1 and 2) while the high-frequency part is placed in the bottom part of the filter (resonators 3 and 4). For the TZs to be generated in between the two passbands, a capacitive coupling using the hook-based structure in Section III-A3 is used in the lower band section between resonators 1 and 2 as shown in Fig. 10 (a). A U-shaped external coupling network is used to couple the SMA probe to both sections simultaneously.

D. Second-Order Diplexer

The detailed geometry of the second-order diplexer is depicted in Fig. 11 using as a basis the CRD in Fig. 4. The structure of the diplexer is similar to the one used in the dual-band BPF where two filtering sections are vertically stacked with a designed AR of 3.78. Each filtering section is comprised of two horizontally iris-coupled resonators. A U-shaped external coupling network is applied in the common port to excite both sections at resonators 2 and 4. For the two output ports, the signal is coupled to the resonators (1 and 3) by directly tapping the SMA probe to the post.

IV. MONOLITHIC INTEGRATION AND EXPERIMENTAL VALIDATION

Using as a basis the design guidelines in Sections II and III, alternative filtering configurations have been designed,

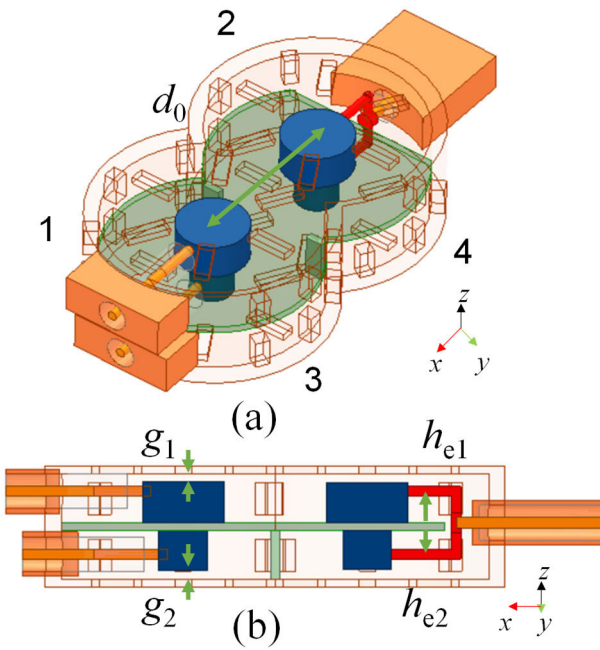


Fig. 11. (a) Geometry of the second-order diplexer, the CRD is shown in Fig. 4. (b) Side view. Geometrical parameters: $a_1 = 5$; $a_2 = 3$; $h = 6$; $g_1 = 1$; $g_2 = 1.2$; $d_0 = 22.7$; $h_{e1} = 3.9$; and $h_{e2} = 3.1$, all units are in mm.

manufactured, and tested. In order for the devices to be monolithically manufactured, particular attention needs to be given to the specifics of the manufacturing process including adding nonresonating slots, selecting the appropriate printing angle, and designing support structures. Their details are summarized as follows.

A. Monolithic Integration

To monolithically manufacture the proposed RF filtering components that simultaneously comprise cavity walls, posts, capacitive coupling elements, and U-shape external coupling elements, nonradiating slots needs to be added on the cavity walls for the metal plating solution to flow inside the cavity volume. The size and location of the slots need to be carefully designed so that they do not produce additional radiation loss or lower Q at the passband frequencies. The slots are placed along the direction of the surface current at the center frequency of the passband, where a detailed discussion of the nonradiating slot design has been presented in [45] and [48].

To facilitate printability using SLA manufacturing, a computer aided design (CAD) model needs to be created to drive the 3-D printer. In this model, the orientation of the filter within the built platform of the printer, the number, and the location of the support structures need to be appropriately selected so that the object to be built is self-supported during the layer-by-layer SLA-based manufacturing process. As shown in Fig. 12(a), the filter is rotated by 90° along the x -axis with its side walls facing the xy plane. External support structures are generated beneath the filter volume which can be readily removed after printing. The perpendicular orientation will also result in better surface roughness [50] of the device. Due to the complexity of the coupling structures, additional inner support structures need to be added inside the

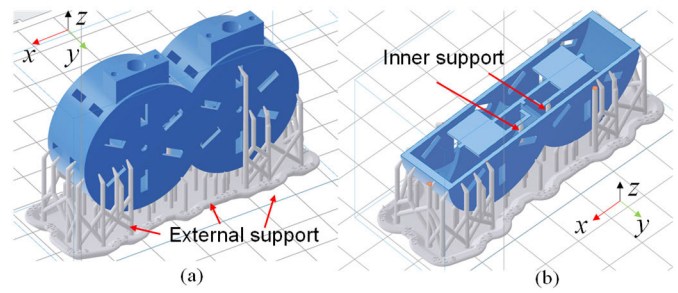


Fig. 12. (a) CAD model for the SLA-based monolithic manufacturing of the four-pole two-TZ BPF showing the required external support structures and printing orientation. (b) Sliced view showing the required inner support structures beneath the capacitive coupling hooks. In these figures, the filter body is shown in blue and the supporting structures are shown in gray.

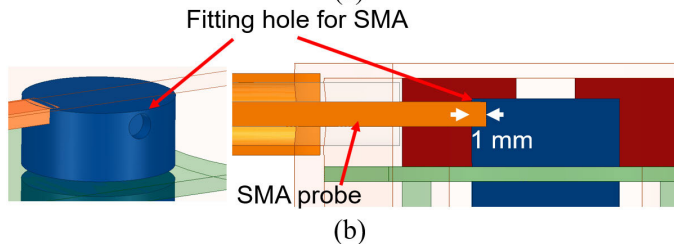
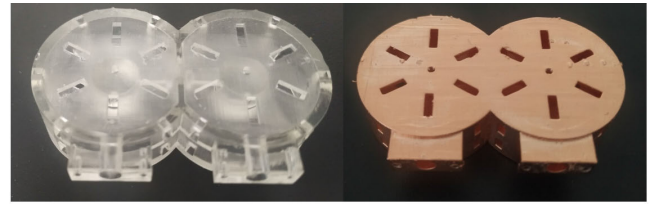


Fig. 13. (a) Manufactured prototype of the four-pole two-TZ filter in Fig. 5. Left: before Cu-plating. Right: after Cu-plating. (b) Details for the fitting hole for SMA probe.

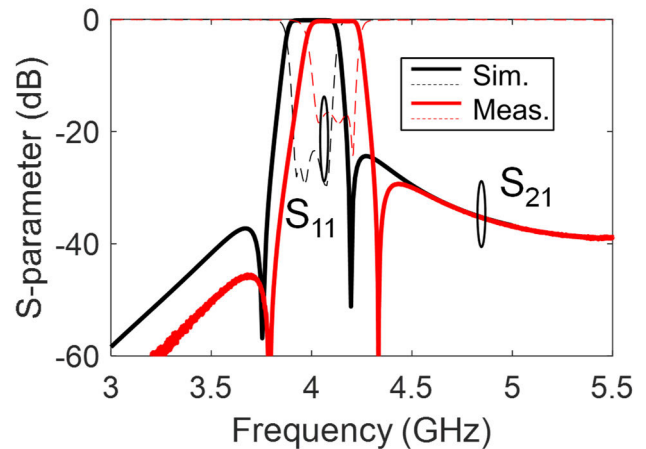


Fig. 14. RF-measured and EM-simulated S -parameters of the four-pole/two-TZ BPF in Fig. 13.

cavity, however at locations where they can be mechanically removed from the nonradiating slots before the metallization process so that the RF component is not short-circuited after plating. The location of the inner support structures is shown in Fig. 12(b). As can be seen, a small number (only two) of support structures has been added to support the capacitive coupling hooks.

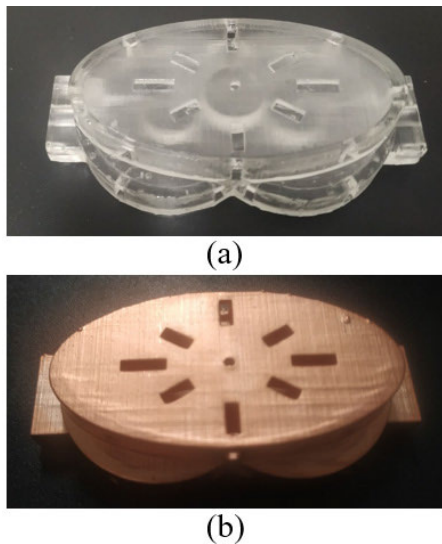


Fig. 15. Manufactured prototype of the three-pole two-TZ in Fig. 8. (a) Before Cu-plating. (b) After Cu-plating.

B. Four-Pole Two-TZ BPF

The SLA-manufactured prototype of the four-pole/two-TZ BPF before and after Cu plating is shown in Fig. 13(a). A commercially available Cu plating process with 50 μm copper thickness ($>20\times$ skin depth at the design frequency) was used. To ensure good contact between the SMA inner conductor and the filter body a fitting hole of 1 mm depth is added to all prototypes as shown in Fig. 13(b). The RF performance was characterized by a Keysight N5224A PNA. The measured EM performance is depicted in Fig. 14 and is summarized as follows: center frequency 4.11 GHz; FBW 6.91%; minimal in-band IL of 0.31 dB; and which corresponds to an effective quality factor (Q_{eff}) of 1320. The frequency shift can be attributed to the fabrication tolerances. Overall, a decent agreement has been achieved between the RF measurements and the EM simulations.

C. Three-Pole Two-TZ BPF

The SLA-printed prototype of the proposed three-pole/two-TZ BPF before and after Cu-plating is shown in Fig. 15(a) and (b). The printing orientation during the AM process is shown in Fig. 16(a). Similar to the four-pole/two-TZ BPF case, the three-pole filter is oriented with its top and bottom wall parallel to the xy plane to minimize the number of support structures. Two inner support structures were used to support the U-shape external coupling network as depicted in Fig. 16(a). The measured RF performance is plotted in Fig. 16(b) and is summarized as follows: center frequency 4.45 GHz; FBW 16.4%; and minimal in-band IL of 0.11 dB ($Q_{\text{eff}} = 1090$). The frequency shift can be attributed to the fabrication tolerances. Overall, a decent agreement has been achieved between the RF measurements and EM simulations.

D. Second-Order Dual-Band BPF

The SLA-printed prototype of the second-order dual-band BPF before and after Cu plating is shown in Fig. 17(a) and (b).

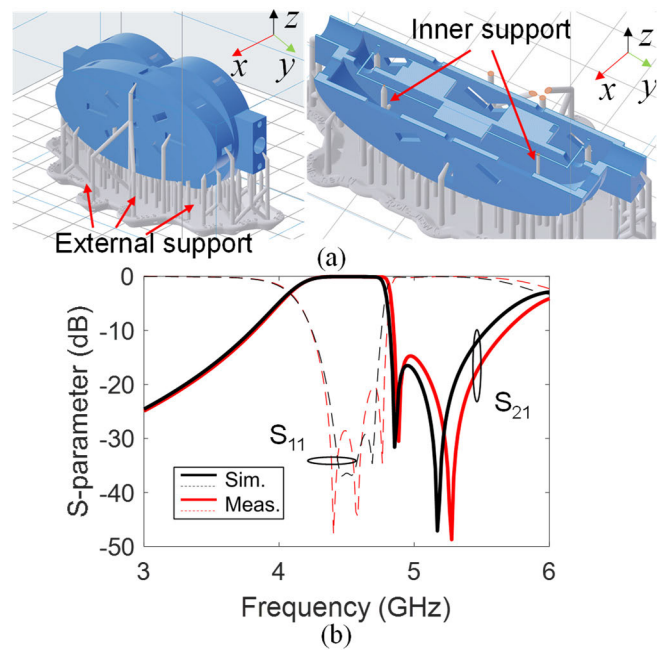


Fig. 16. (a) CAD model for the SLA-based monolithic manufacturing of the three-pole two-TZ BPF in Fig. 8. (b) RF-measured and EM-simulated S -parameters of the three-pole two-TZ BPF in Fig. 15.

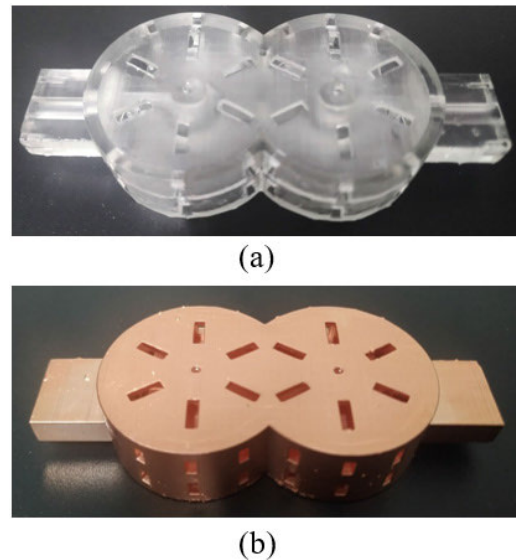


Fig. 17. Manufactured prototype of the second-order dual-band BPF in Fig. 10. (a) Before Cu-plating. (b) After Cu-plating.

The printing orientation during the AM process is shown in Fig. 18(a). Two inner support structures were also used in this case to support the U-shape external coupling network as depicted in Fig. 18(a) and they are removed after manufacturing. The measured EM performance of the dual-band BPF is shown in Fig. 18(b) and is summarized as follows: for the lower band, center frequency $f_1 = 3.54$ GHz, FBW = 5.8%, minimal in-band IL = 0.37 dB ($Q_{\text{eff}} = 700$). For the higher band, center frequency $f_2 = 4.63$ GHz, FBW = 7.7%, and minimal in-band IL = 0.28 dB ($Q_{\text{eff}} = 710$). The measured FBW for the lower band is smaller than the simulated one,

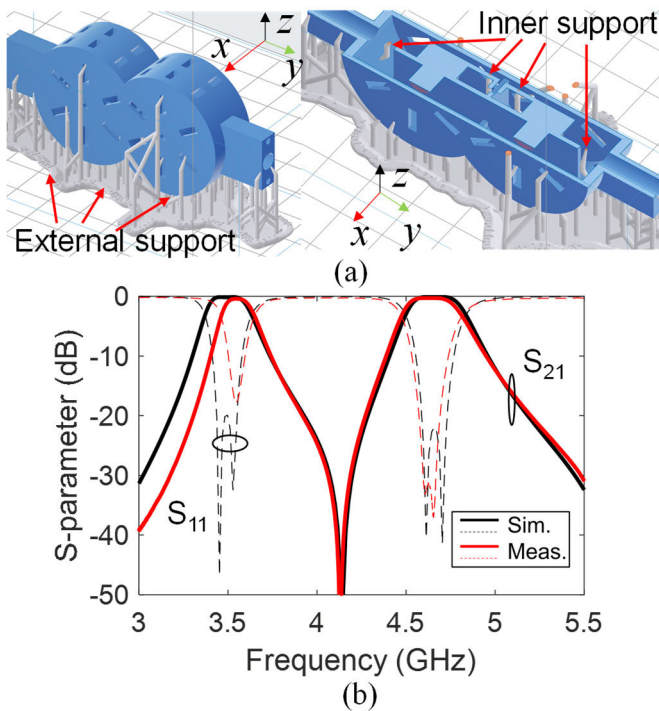


Fig. 18. (a) CAD model for SLA-based monolithic manufacturing of two-pole dual-band BPF in Fig. 10. (b) RF-measured and EM-simulated S -parameters of the two-pole dual-band BPF in Fig. 17.

which is attributed to the manufacturing tolerances at the iris width.

E. Second-Order Diplexer

The SLA-printed prototype of the second-order diplexer before and after Cu plating is shown in Fig. 19(a) and (b) and the CAD model for SLA manufacturing is depicted in Fig. 20(a). It should be noted that two 90° bend SMA adaptors were used in the two output ports to facilitate the RF measurement as shown in Fig. 19(c), where the loss of the adaptors has been calibrated out. The measured EM performance of the second-order diplexer is shown in Fig. 20(b) and is summarized as follows: for the lower band, center frequency $f_1 = 3.9$ GHz, FBW = 8.35%, minimal in-band IL = 0.35 dB ($Q_{\text{eff}} = 850$). For the higher band, center frequency $f_2 = 5.1$ GHz, FBW = 7%, minimal in-band IL = 0.22 dB ($Q_{\text{eff}} = 1020$). A good agreement has been achieved between the RF measurements and EM simulations, successfully validating the proposed compact monolithic integrated filter concept.

F. Comparison With State-of-the-Art

A comparison with state-of-the-art CNC- and SLA-manufactured coaxial cavity resonator-based filters is provided in Table I. As can be seen, the majority of the coaxial cavity filters that have been presented in the open technical literature are based on split-blocks of all-metal CNC machined parts that are assembled with screws. Although SLA AM-based integration schemes have been proposed to produce devices with less weight and cost, most of them rely

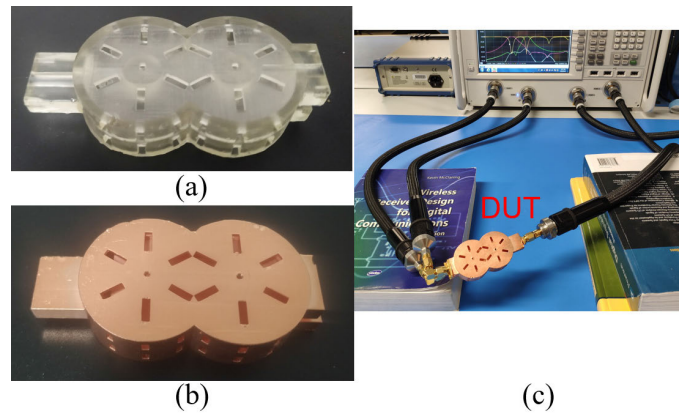


Fig. 19. Manufactured prototype of the second-order diplexer in Fig. 11. (a) Before Cu-plating. (b) After Cu-plating. (c) Measurement setup.

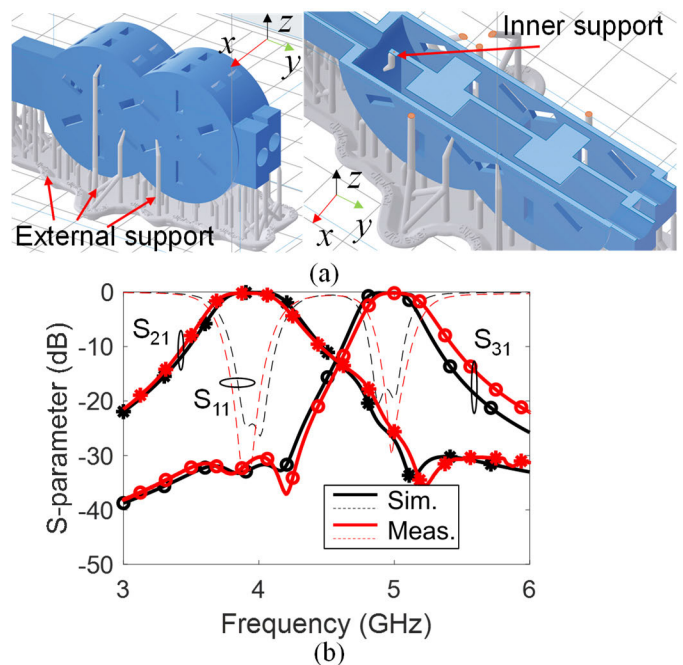


Fig. 20. (a) CAD model for SLA-based monolithic manufacturing of the second-order diplexer. (b) RF-measured and EM-simulated S -parameters of the second-order diplexer in Fig. 19.

on split-block integration schemes that require multiple parts to be printed and postassembled, which can induce radiation losses and lower Q_{eff} e.g., 100 in [29] and [44]. In addition, the split-block CNC or SLA integration schemes require additional mechanical parts to be added for the assembly screws, which significantly increase the size and the weight of the BPF. In this work, the monolithic SLA-based integration approach work has resulted in remarkably higher Q_{eff} (as high as 1320) as well as eliminated the need for assembly screws. Furthermore, the proposed vertically-stacked approach has resulted in more compact filter structures with ARs as small as 3.7–4, whereas the conventional in-line coaxial filters usually have an AR above 10 e.g., 11.2 in [44] and 17 in [48]. It should be noticed that the listed ARs in the reference are the minimal values based on the reported internal size that do

TABLE I
STATE-OF-ART COAXIAL CAVITY RESONATOR-BASED FILTERS

Ref.	Ver.	Mo.	Tech.	#Res.	Func.	Freq (GHz)	FBW%	AR	IL (dB)	Q_{eff}
[13]	No	No	CNC	6	Single	1.55	3.9	>5.28	N/A	4400
[22]	Yes	No	CNC	4	Dual	2.6/3.6	8	>4.04	0.28/0.34	1500
[23]	No	No	CNC	3	Dual	0.9/1.8	30/15	>3.39	0.22/0.25	1500
[30]	Yes	No	SLA	4	Single	1.7	10	>2.39	1.3	100*
[31]	Yes	Yes	SLA	3	Single	3.51	6.7	1.54	0.09	2461
[44]	No	No	SLA	5	Tunable	1.3-1.77	4.8-12.3	>11.2	2.7-6.1	100*
[48]	No	Yes	SLA	6	Dual	3.7/4	4.9/3.3	17	0.32/0.34	1300
[51]	No	No	CNC	9	Tunable	1.98-2.02	1-4	>10	N/A	200
[52]	No	No	CNC	5	Single	2.8	10.7	>5.4	0.56	300*
TW	Yes	Yes	SLA	4	Single	4.11	6.9	4.07	0.31	1320
TW	Yes	Yes	SLA	3	Single	4.45	16.4	3.72	0.12	1090
TW	Yes	Yes	SLA	4	Dual	3.5/4.6	5.8/7.7	3.93	0.37/0.28	>700
TW	Yes	Yes	SLA	4	Diplexer	3.9/5.1	8.3/7.0	3.78	0.35/0.22	>850

(Ver.: vertical stack, Mo.: monolithic, Func.: functionality TW: This work, N/A: not applicable, #Res.: number of resonators. * indicates approximate values, the listed AR of the reference are the minimal values based on the reported internal sizes excluding the assembly screws)

not include the assembly screws i.e., the practical AR in the reference is larger than the listed value.

Although two-layer vertically-stacked structures have been presented in [22], [28], [29], and [30], they are either based on conventional CNC machined parts [22], [30] or split-block AM [28], [29] assemblies and they are less complex than the geometrical configurations shown in this work. Specifically, when compared to the filter concept in [30], the proposed vertically-stacked coaxial BPF concept is distinctively different. The work in [30] discusses a filter design based on the bottom coupling between a coaxial resonator and TE-mode dielectric resonator which is assembled using split blocks. Furthermore, compared to the BPF in [29] where TZs are generated using cross couplings, this work proposed a new type of CRD to facilitate TZ generation by super-positioning two filtering paths as validated by the three-pole/two-TZ BPF. With regard to the dual-band BPF in [22], the filter in this work exhibits a TZ between the two passbands to improve the isolation due to the use of different coupling elements in the two filtering sections. Compared to the authors' prior work in [45], [46], [47], [48], and [49], the filters presented in this work exhibit a significantly higher level of complexity including the combination of vertical-stacking, cross-coupling, positive, and negative coupling elements. Furthermore, novel external coupling structures, resulting in filtering components with higher order, and advanced transfer functions have been demonstrated. Moreover, the concept has been shown for highly-miniaturized vertically-stacked diplexers that are demonstrated in this work for the first time. To the best of the authors' knowledge, the proposed monolithic vertical SLA-based integration design approach is the only one

demonstrated for BPFs with a high number of resonators, RF diplexers, and multiband BPF configurations.

V. CONCLUSION

This manuscript discussed the design, manufacturing, and experimental testing of ultra-miniaturized monolithically-integrated coaxial cavity resonator-based single-band/ multi-band RF filters and RF diplexers. By using a vertically-stacked resonator integration approach, the following unique characteristics can be obtained: 1) small physical size enabled by vertical stacking and low-profile capacitively-loaded coaxial cavity resonators and by monolithic integration; 2) multiple TZs that increase the passband selectivity due to the geometrical arrangements of the resonators that facilitate the realization of cross-couplings; and 3) versatile transfer function e.g., single band and multiband BPFs with TZs, and diplexer. To validate the proposed concept, a four-pole/two TZs BPF, a three-pole/two TZs BPF, a second-order dual-band BPF, and a second-order diplexer operating at C-band were designed, manufactured, and tested.

REFERENCES

- [1] R. V. Snyder, G. Macchiarella, S. Bastioli, and C. Tomassoni, "Emerging trends in techniques and technology as applied to filter design," *IEEE J. Microw.*, vol. 1, no. 1, pp. 317-344, Jan. 2021.
- [2] H. Wang and Q.-X. Chu, "Generation of transmission zero through electric and magnetic mixed coupling," in *Proc. Int. Conf. Microw. Millim. Wave Technol.*, Guilin, China, Apr. 2007, pp. 1-3.
- [3] J.-K. Xiao, M. Zhu, Y. Li, L. Tian, and J.-G. Ma, "High selective microstrip bandpass filter and diplexer with mixed electromagnetic coupling," *IEEE Microw. Wireless Compon. Lett.*, vol. 25, no. 12, pp. 781-783, Dec. 2015.

- [4] C. Tomassoni and R. Sorrentino, "A new class of pseudo-elliptic waveguide filters using resonant posts," in *IEEE MTT-S Int. Microw. Symp. Dig.*, Montreal, QC, Canada, Jun. 2012, pp. 1–3.
- [5] S. Amari and G. Macchiarella, "Synthesis of inline filters with arbitrarily placed attenuation poles by using nonresonating nodes," *IEEE Trans. Microw. Theory Techn.*, vol. 53, no. 10, pp. 3075–3081, Oct. 2005.
- [6] G. Macchiarella, S. Bastioli, and R. V. Snyder, "Design of in-line filters with transmission zeros using strongly coupled resonators Pairs," *IEEE Trans. Microw. Theory Techn.*, vol. 66, no. 8, pp. 3836–3846, Aug. 2018.
- [7] S. Bastioli, R. V. Snyder, and G. Macchiarella, "Design of in-line filters with strongly coupled resonator triplet," *IEEE Trans. Microw. Theory Techn.*, vol. 66, no. 12, pp. 5585–5592, Dec. 2018.
- [8] D. Lu, B. Zhu, and M. Yu, "Synthesis approach to planar filter design using new cascade hybrid triplet block with arbitrary-placed TZ pair," *IEEE Trans. Microw. Theory Techn.*, vol. 70, no. 4, pp. 2196–2206, Apr. 2022.
- [9] R. R. Mansour, "Filter technologies for wireless base stations," *IEEE Microw. Mag.*, vol. 5, no. 1, pp. 68–74, Mar. 2004.
- [10] D. Liang, X. Zhang, B. Yang, and D. Young, "Overview of base station requirements for RF and microwave filters," in *IEEE MTT-S Int. Microw. Symp. Dig.*, Perugia, Italy, Nov. 2021, pp. 46–49.
- [11] J. B. Thomas, "Cross-coupling in coaxial cavity filters—A tutorial overview," *IEEE Trans. Microw. Theory Techn.*, vol. 51, no. 4, pp. 1368–1376, Apr. 2003.
- [12] M. Hoft and F. Yousif, "Orthogonal coaxial cavity filters with distributed cross-coupling," *IEEE Microw. Wireless Compon. Lett.*, vol. 21, no. 10, pp. 519–521, Oct. 2011.
- [13] Y. Wang and M. Yu, "True inline cross-coupled coaxial cavity filters," *IEEE Trans. Microw. Theory Techn.*, vol. 57, no. 12, pp. 2958–2965, Dec. 2009.
- [14] M. Pal and R. Ghatak, "A distinctive resonance: Multiband bandpass filter design techniques using multimode resonators," *IEEE Microw. Mag.*, vol. 16, no. 11, pp. 36–55, Dec. 2015.
- [15] R. Gómez-García and A. C. Guyette, "Reconfigurable multi-band microwave filters," *IEEE Trans. Microw. Theory Techn.*, vol. 63, no. 4, pp. 1294–1307, Apr. 2015.
- [16] M. Fan, K. Song, L. Yang, and R. Gomez-Garcia, "Balanced-circuit-based dual-band bandpass filter with symmetrical reflectionless behavior," in *Proc. IEEE Radio Wireless Symp. (RWS)*, San Diego, CA, USA, Jan. 2021, pp. 141–143.
- [17] S. Amari and M. Bekheit, "A new class of dual-mode dual-band waveguide filters," *IEEE Trans. Microw. Theory Techn.*, vol. 56, no. 8, pp. 1938–1944, Aug. 2008.
- [18] E. Doumanis and G. Goussetis, "Dual-frequency combline resonators for four-port bandpass filters," in *Proc. 48th Eur. Microw. Conf. (EuMC)*, Madrid, Spain, Sep. 2018, pp. 659–662.
- [19] X. Liu, L. P. B. Katehi, and D. Peroulis, "Novel dual-band microwave filter using dual-capacitively-loaded cavity resonators," *IEEE Microw. Wireless Compon. Lett.*, vol. 20, no. 11, pp. 610–612, Nov. 2010.
- [20] Y. Wu, R. Gajaweera, and J. Everard, "Dual-band bandpass filter using coaxial stepped impedance resonators," in *Proc. Int. Conf. Students Appl. Eng. (ISCAE)*, Oct. 2016, pp. 181–185.
- [21] F.-C. Chen, J.-M. Qiu, S.-W. Wong, and Q.-X. Chu, "Dual-band coaxial cavity bandpass filter with helical feeding structure and mixed coupling," *IEEE Microw. Wireless Compon. Lett.*, vol. 25, no. 1, pp. 31–33, Jan. 2015.
- [22] E. Doumanis, L. Guan, G. Goussetis, and D. Ferling, "Dual-band bandpass double ground plane coaxial resonators and filters," *IEEE Trans. Microw. Theory Techn.*, vol. 66, no. 8, pp. 3828–3835, Aug. 2018.
- [23] J. A. Ruiz-Cruz, M. M. Fahmi, and R. R. Mansour, "Triple-conductor combline resonators for dual-band filters with enhanced guard-band selectivity," *IEEE Trans. Microw. Theory Techn.*, vol. 60, no. 12, pp. 3969–3979, Dec. 2012.
- [24] Y. Xie, F.-C. Chen, Q.-X. Chu, and Q. Xue, "Dual-band coaxial filter and diplexer using stub-loaded resonators," *IEEE Trans. Microw. Theory Techn.*, vol. 68, no. 7, pp. 2691–2700, Jul. 2020.
- [25] G. L. Matthaei, "Comb-line band-pass filters of narrow or moderate bandwidth," *Microw. J.*, vol. 6, pp. 82–91, Aug. 1963.
- [26] S. Bulja, E. Doumanis, and D. Kozlov, "Concentric distributed resonators and filters," in *Proc. IEEE Radio Wireless Symp. (RWS)*, Anaheim, CA, USA, Jan. 2018, pp. 267–269.
- [27] S. Bulja and M. Gimersky, "Low-profile distributed cavity resonators and filters," *IEEE Trans. Microw. Theory Techn.*, vol. 65, no. 10, pp. 3769–3779, Oct. 2017.
- [28] E. Lopez-Oliver et al., "3-D printed bandpass filter using conical posts interlaced vertically," in *IEEE MTT-S Int. Microw. Symp. Dig.*, Los Angeles, CA, USA, Aug. 2020, pp. 580–582.
- [29] E. Lopez-Oliver et al., "3-D-Printed compact bandpass filters based on conical posts," *IEEE Trans. Microw. Theory Techn.*, vol. 69, no. 1, pp. 616–628, Jan. 2021.
- [30] M. Hoft, "Bottom coupling of combline resonators for hybrid dielectric/air-cavity bandpass filters," in *Proc. Eur. Microw. Conf.*, Manchester, U.K., Sep. 2006, pp. 1323–1326.
- [31] K. Zhao and D. Psychogiou, "A monolithic vertical integration concept for compact coaxial-resonator-based bandpass filters using additive manufacturing," *IEEE Microw. Wireless Compon. Lett.*, vol. 31, no. 6, pp. 689–692, Jun. 2021.
- [32] T.-H. Chio, G.-L. Huang, and S.-G. Zhou, "Application of direct metal laser sintering to waveguide-based passive microwave components, antennas, and antenna arrays," *Proc. IEEE*, vol. 105, no. 4, pp. 632–644, Apr. 2017.
- [33] B. Zhang and H. Zirath, "A metallic 3-D printed e-band radio front end," *IEEE Microw. Wireless Compon. Lett.*, vol. 26, no. 5, pp. 331–333, May 2016.
- [34] C. R. Garcia, R. C. Rumpf, H. H. Tsang, and J. H. Barton, "Effects of extreme surface roughness on 3D printed horn antenna," *Electron. Lett.*, vol. 49, no. 12, pp. 734–736, 2013.
- [35] F. Calignano, D. Manfredi, E. P. Ambrosio, L. Iuliano, and P. Fino, "Influence of process parameters on surface roughness of aluminum parts produced by DMLS," *Int. J. Adv. Manuf. Technol.*, vol. 67, nos. 9–12, pp. 2743–2751, Aug. 2013.
- [36] G. P. Le Sage, "3D printed waveguide slot array antennas," *IEEE Access*, vol. 4, pp. 1258–1265, 2016.
- [37] C. Guo, X. Shang, J. Li, F. Zhang, M. J. Lancaster, and J. Xu, "A lightweight 3-D printed X-band bandpass filter based on spherical dual-mode resonators," *IEEE Microw. Wireless Compon. Lett.*, vol. 26, no. 8, pp. 568–570, Aug. 2016.
- [38] W. J. Otter and S. Lucyszyn, "3-D printing of microwave components for 21st century applications," in *IEEE MTT-S Int. Microw. Symp. Dig.*, Chengdu, China, Jul. 2016, pp. 1–3.
- [39] J. Li, C. Guo, L. Mao, J. Xiang, G.-L. Huang, and T. Yuan, "Monolithically 3-D printed hemispherical resonator waveguide filters with improved out-of-band rejections," *IEEE Access*, vol. 6, pp. 57030–57048, 2018.
- [40] K. Y. Chan, R. Ramer, and R. Sorrentino, "Low-cost Ku-band waveguide devices using 3-D printing and liquid metal filling," *IEEE Trans. Microw. Theory Techn.*, vol. 66, no. 9, pp. 3993–4001, Sep. 2018.
- [41] D. Miek, S. Simmich, F. Kamrath, and M. Hoft, "Additive manufacturing of E-plane cut dual-mode X-band waveguide filters with mixed topologies," *IEEE Trans. Microw. Theory Techn.*, vol. 68, no. 6, pp. 2097–2107, Jun. 2020.
- [42] C. Carceller, F. Gentili, W. Bosch, D. Reichartzeder, and M. Schwenzenwein, "Ceramic additive manufacturing as an alternative for the development of miniaturized microwave filters," in *IEEE MTT-S Int. Microw. Symp. Dig.*, Pavia, Italy, Sep. 2017, pp. 1–3.
- [43] G. Venanzoni, M. Dionigi, C. Tomassoni, and R. Sorrentino, "3-D-printed quasi-elliptical evanescent mode filter using mixed electromagnetic coupling," *IEEE Microw. Wireless Compon. Lett.*, vol. 28, no. 6, pp. 497–499, Jun. 2018.
- [44] D. Psychogiou and M. Deng, "High-order coaxial bandpass filters with multiple levels of transfer function tunability," *IEEE Microw. Wireless Compon. Lett.*, vol. 30, no. 4, pp. 367–370, Apr. 2020.
- [45] K. Zhao and D. Psychogiou, "Monolithic SLA-based capacitively-loaded high-Q coaxial resonators and bandpass filters," in *Proc. 50th Eur. Microw. Conf. (EuMC)*, Utrecht, The Netherlands, Jan. 2021, pp. 471–474.
- [46] K. Zhao and D. Psychogiou, "Spurious suppression techniques for 3-D printed coaxial resonator bandpass filters," *IEEE Microw. Wireless Compon. Lett.*, vol. 32, no. 1, pp. 33–36, Jan. 2022.
- [47] K. Zhao and D. Psychogiou, "Monolithically-integrated 3D printed coaxial bandpass filters and RF diplexers: Single-band and dual-band," *Int. J. Microw. Wireless Technol.*, vol. 14, no. 3, pp. 293–304, Apr. 2022.
- [48] K. Zhao and D. Psychogiou, "Monolithic multiband coaxial resonator-based bandpass filter using stereolithography apparatus (SLA) manufacturing," *IEEE Trans. Microw. Theory Techn.*, vol. 70, no. 9, pp. 4156–4166, Sep. 2022.
- [49] K. Zhao and D. Psychogiou, "Monolithically integrated coaxial resonator-based filtennas using SLA three-dimensional printing," *IEEE Antennas Wireless Propag. Lett.*, vol. 22, no. 1, pp. 189–193, Jan. 2023.

- [50] C. Arnold, D. Monsees, J. Hey, and R. Schweyen, "Surface quality of 3D-printed models as a function of various printing parameters," *Materials*, vol. 12, no. 12, p. 1970, Jun. 2019.
- [51] M. Yuceer, "A reconfigurable microwave combline filter," *IEEE Trans. Circuits Syst. II, Exp. Briefs*, vol. 63, no. 1, pp. 84–88, Jan. 2016.
- [52] M. S. Anwar and H. R. Dhanyal, "Design of S-band combline coaxial cavity bandpass filter," in *Proc. 15th Int. Bhurban Conf. Appl. Sci. Technol. (IBCAST)*, Islamabad, Pakistan, Jan. 2018, pp. 866–869.



Kunchen Zhao (Graduate Student Member, IEEE) received the bachelor's degree from the University of Electronic Science and Technology of China, Chengdu, China, in 2018, and the master's degree from Ohio State University, Columbus, OH, USA, in 2019, both in electrical engineering. He is currently pursuing the Ph.D. degree in RF/microwave engineering at the University of Colorado Boulder, Boulder, CO, USA.

His main research interests are the design of high-performance RF passive circuits.



Dimitra Psychogiou (Senior Member, IEEE) received the Dipl.-Eng. degree in electrical and computer Engineering from the University of Patras, Patras, Greece, in 2008, and the Ph.D. degree in electrical engineering from the Swiss Federal Institute of Technology (ETH), Zürich, Switzerland, in 2013.

Prior to joining University College Cork (UCC), she was a Sr. Research Scientist with Purdue University, West Lafayette, IN, USA, and an Assistant Professor with the University of Colorado Boulder (UC Boulder), Boulder, CO, USA. She is currently

a Professor of electrical and electronic engineering with the UCC and the Tyndall National Institute, Cork, Ireland. Her research has been presented in more than 200 publications. Her current research interests include RF design and characterization of reconfigurable microwave and millimeter-wave passive components, RF-MEMS, acoustic wave resonator-based filters, tunable filter synthesis, frequency-agile antennas, and additive manufacturing technologies for 3-D antenna subsystems.

Prof. Psychogiou is a Senior Member of International Union for Radio Science (URSI) and a member of the IEEE MTT-S Filters and Passive Components (MTT-5) and Microwave Control Materials and Devices (MTT-13) Committees. She has received the 2021 Roberto Sorrentino Prize, the SFI Research Professorship Award, the 2020 NSF CAREER Award, the 2020 URSI Young Scientist Award, and the Junior Faculty Outstanding Research Award from UC Boulder. Furthermore, she serves on the Technical Review Board of various IEEE and EuMA conferences and journals and is the Chair of MMT-13 and the Secretary of United States National Committee (USNC)-URSI Commission D. She is an Associate Editor of the IEEE MICROWAVE AND WIRELESS COMPONENTS LETTERS and the *International Journal of Microwave and Wireless Technologies*. Previously, she was an Associate Editor of the IET Microwaves, Antennas and Propagation journal.